Modelling the solidification of ductile cast iron parts with varying wall thicknesses

Bjerre, Mathias Karsten; Tiedje, Niels Skat; Thorborg, Jesper; Hattel, Jesper Henri

Published in:
I O P Conference Series: Materials Science and Engineering

Link to article, DOI:
10.1088/1757-899X/84/1/012038

Publication date:
2015

Document Version
Publisher's PDF, also known as Version of record

Modelling the solidification of ductile cast iron parts with varying wall thicknesses

2015 IOP Conf. Ser.: Mater. Sci. Eng. 84 012038

(http://iopscience.iop.org/1757-899X/84/1/012038)

Modelling the solidification of ductile cast iron parts with varying wall thicknesses

M Bjerre[1], N S Tiedje[1] J Thorborg[2] & J H Hattel[1]

[1] Department of Mechanical Engineering, Technical University of Denmark
[2] Magma GmbH

E-mail: makabj@mek.dtu.dk

Abstract. In the present paper modelling the solidification of cast iron parts is considered. Common for previous efforts in this field is that they have mainly considered thin walled to medium thickness castings. Hence, a numerical model combining the solidification model presented by Lesoult et al. [1] with a 2D FE solution of the heat conduction equation is developed in an in-house code and model parameters are calibrated using experimental data from representative castings made of ductile cast iron. The main focus is on the influence of casting thickness and resulting local cooling conditions on the solidification pattern and the relation to formation of degenerate graphite.

1. Introduction

Ductile cast iron (DCI) is widely used in the automotive industry but also for parts in wind turbines (bed frame, main shaft and rotor hub) due to the combination of good mechanical properties and low cost. In heavy sections, however, degenerate graphite morphologies might form reducing ductility and fatigue strength of the part. A wide range of factors have been found to influence the formation of degenerate graphite as reviewed by Källbom et al. [2] and the mechanisms describing its formation are still not fully understood.

One of the factors known to be important is the thermal conditions. Slow cooling rates are often associated with the formation of degenerate graphite and the degenerate morphology mainly appears at the thermal centre of heavy sections. The cooling curves measured from heavy castings usually also show distinct features not seen in ordinary DCI castings, [3], such as up to three arrests associated with primary solidification, initial limited eutectic growth and bulk eutectic growth.

In this paper, we validate a model combining a temperature solver and the microstructural model originally proposed by Lesoult et al. [1] and further developed by Pedersen et al. [4]. This is done by comparing temperature curves and nodule counts from the simulation to experimental data from bars with cross sections of 34.7 mm × 34.7 mm, 52 mm × 52 mm and 65 mm × 65 mm. We then use our validated model to simulate a thick-walled part of cross section 300 mm × 300 mm in order to study the solidification pattern and thermal gradients the part experiences during solidification as the thermal conditions are at present believed to play a major role for the formation and distribution of porosities, [5], and may also be significant for formation of degenerate graphite. The model does not describe these phenomena but the overall solidification pattern including temperature fields is nevertheless of interest in this relation.

2. Experimental data

A series of experiments were carried out where bars of different thermal moduli were cast from a high-silicon melt. The experiment is presented elsewhere, Vedel-Smith et al. [6], and we will only present it briefly: Bars in three sizes were produced using a scalable model where the length of the bar is 3 times the length of the two remaining sides. The side lengths were 34.7 mm, 52 mm and 65 mm producing bars of thermal moduli 8 mm, 10 mm and 15 mm respectively. The dimensions of the bars allow us to treat the bars as two dimensional objects in the sense that it is reasonable to assume that the thermal variations in the length direction of the bar are negligible. The bars were cast from a hypereutectic high-silicon melt, see table 1 and the temperature was measured at the centre of each bar using a k-type thermocouple. Microstructural data in terms of nodule number densities were obtained from castings of side lengths 52 mm and 65 mm, however not from those in which the temperature was measured. The compositional variations between the castings were however small and will have limited effect on the conclusions to be drawn here.

Table 1. Alloy composition [%wt], carbon equivalent (CE) and casting temperature [6].

CE	C	Si	Casting T [°C]
4.57	3.31	3.81	1387

3. Numerical Model

A two dimensional thermal model has been set up for casting and mould and it is coupled to a microstructural model that describes the solidification of the casting. The casting domain is a quarter of a bar cross section, see Fig. 1, and is discretised using 10 by 10 elements for the smallest bar and 20 by 20 for the largest. The total size of the domain is 150 mm by 150 mm. Convective cooling is applied on the two sides which represent the outside of the mould while adiabatic boundary conditions are applied at the remaining two sides representing internal symmetry lines.

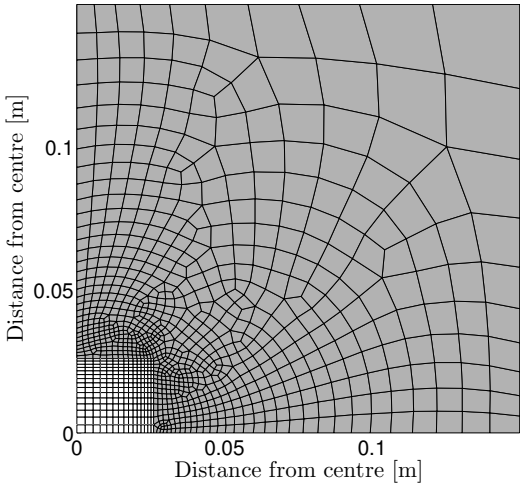

Figure 1. Calculation domain for the casting with side lengths of 52 mm. The shaded area and the white area represent the mould and the casting, respectively. Adiabatic boundary conditions are applied on left and bottom boundaries and convective cooling on the right and top boundaries. The mesh was generated using ABAQUS.

Microstructural model

The microstructural developments during solidification are described using the model developed by Lesoult et al. [1, 7]. In the case of a hypereutectic melt, the model predicts the nucleation

of primary graphite forming as the first solid phase in the melt. The nucleation is described by a modified version of Oldfield's model in which the rate of nucleation, ΔN_i, is determined by the change of the undercooling with respect to the graphite liquidus, ΔT_L^g, and the remaining liquid volume, V^{liq}, in the element:

$$\mathrm{d}N_i = \begin{cases} A_n(\Delta T_L^g)^{n-1} \cdot V^{\text{liq}} \frac{\mathrm{d}\Delta T_L^g}{\mathrm{d}t}\mathrm{d}t & \text{if} \quad \frac{\mathrm{d}\Delta T_L^g}{\mathrm{d}t} > 0 \\ 0 & \text{else} \end{cases} \tag{1}$$

where A_n is a constant related to the exponent n, which is set to 1 in this and previous works [7, 4]. The nodules nucleated at time point i then represent a family of nodules which will grow by the same rates. This is a reasonable assumption as two nodules nucleated simultaneously in the same volume element will experience the same growth conditions with this model.

As the volume reaches the austenite liquidus determined by the phase diagram, the nodules are immediately encapsulated in an austenite shell of a predefined thickness δr^γ as is any new nodule nucleated from this point on. As soon as the eutectic solidification has started the nodules grow only by diffusion of carbon through the austenite shells, while the shell is in direct contact with the melt. The dynamic equations for the radius of the graphite nodule, r^g, and the austenite shell, r^γ, during eutectic solidification are described by

$$\frac{\mathrm{d}r^g}{\mathrm{d}t} = \frac{\rho^\gamma}{\rho^g} D_C^\gamma \frac{1}{1 - w_C^{\gamma/g}} \frac{r^\gamma}{(r^\gamma - r^g) r^g} (w_C^{\gamma/l} - w_C^{\gamma/g}) \tag{2}$$

$$\frac{\mathrm{d}r^\gamma}{\mathrm{d}t} = \frac{D_C^\gamma r^g}{(r^\gamma - r^g) r^\gamma} \frac{w_C^{\gamma/l} - w_C^{\gamma/g}}{w_C^{l/\gamma} - w_C^{\gamma/l}} \left(1 + \frac{\rho^\gamma - \rho^g}{\rho^g} \frac{w_C^{l/\gamma} - w_C^{\gamma/l}}{1 - w_C^{\gamma/g}}\right) + \Delta(r^\gamma) \tag{3}$$

with

$$\Delta(r^\gamma) = \begin{cases} \frac{1}{m_C^\gamma} \frac{\partial T}{\partial t} \frac{\Phi \cdot \frac{1}{3}\left(\rho^l ({}^o r)^3 - \rho^g (r^g)^3 - \rho^\gamma ((r^\gamma)^3 - (r^g)^3)\right)}{(r^\gamma)^2 \rho^\gamma (w_C^{l/\gamma} - w_C^{\gamma/l})} & \text{if} \quad V^\gamma \leq 0 \\ 0 & \text{if} \quad V^\gamma > 0 \end{cases}$$

$$\Phi = \frac{\rho^l (1 - f^\gamma) + \rho^\gamma f^\gamma k_C}{\rho^l (1 - f^\gamma) + \rho^\gamma f^\gamma}$$

where ρ^ϕ is the density of phase ϕ, $w_C^{\phi/\theta}$ is the carbon content in phase ϕ in equilibrium with phase θ. D_C^γ is the diffusion coefficient of carbon diffusing in austenite. In $\Delta(r^\gamma)$, m_C^γ is the slope of the austenite liquidus, k_C is the partition coefficient and ${}^o r$ is the average distance between nodules. Further, f^γ is the fraction of the off-eutectic volume which is austenite.

During solidification, eutectic spheres will increasingly impinge reducing the actual growth compared to the rates described by Eq. 2 and 3. This is taken into account by multiplying the growth rates of the total eutectic and graphite volume in the element by the Avrami correction factor $\psi = 1 - f^s$, f^s being the fraction solid, [7],

$$\frac{\mathrm{d}V^{\text{Eut}}}{\mathrm{d}t} = \sum_i \Delta N_i (r^\gamma)^2 \frac{\mathrm{d}r^\gamma}{\mathrm{d}t} \psi \qquad \frac{\mathrm{d}V^g}{\mathrm{d}t} = \sum_i \Delta N_i (r^g)^2 \frac{\mathrm{d}r^g}{\mathrm{d}t} \psi \tag{4}$$

where the sum is over the nucleation events and V^{Eut} and V^g are the total eutectic and graphite volume of an element respectively. Nucleation and growth of nodules reduce the carbon content of the melt which in some cases is compensated for by sufficient growth of the eutectic austenite keeping the carbon content of the liquid at the austenite liquidus. In other cases, especially when the cooling is strong, the growth of eutectic austenite will not be sufficient. The model

then predicts the growth of off-eutectic austenite dendrites to keep the melt in equilibrium with austenite giving a growth rate of off-eutectic austenite of

$$\frac{\mathrm{d}f^{\gamma}}{\mathrm{d}t} = \frac{-X_C}{(1-k_C)w_C^l} + \frac{\Phi}{(1-k_C)w_C^l}\frac{1}{m_C^{\gamma}}\frac{\mathrm{d}T}{\mathrm{d}t} \tag{5}$$

$$X_C = \frac{-\rho^{\gamma}w_C^l[1-\Phi]\left(\frac{\mathrm{d}V^{\mathrm{Eut}}}{\mathrm{d}t} - \frac{\mathrm{d}V^g}{\mathrm{d}t}\right) - (\rho^{\gamma}-\rho^g)[(1-\Phi)w_C^l + w_C^{\gamma/g} - w_C^{\gamma/l}]\frac{\mathrm{d}V^g}{\mathrm{d}t}}{\rho^l V^{\circ} - \rho^g V^g - \rho^{\gamma}(V^{\mathrm{Eut}} - V^g)}$$

where w_C^l is the carbon content of the liquid phase.

Thermal model
Heat transfer is modelled using a 2D finite element thermal solver. The description of the heat transfer coefficient (HTC) across the casting-mould interface and the coupling to the microstructural model is done as described by Pedersen et al. [4]: The HTC is made dependent on the fraction solid of the surface elements of the casting, with an initial value of 1500 W/m^{2}K ending at 300 W/m^{2}K when the fraction solid reaches 0.4. The latent heat from solidification is released mainly through a direct source term but also partly through a modified ρc_p in the heat conduction equation: The heat conduction equation with constant material properties is given as

$$\rho c_p \frac{\mathrm{d}T}{\mathrm{d}t} = k\nabla^2 T + \dot{Q}''' \tag{6}$$

where ρ in this case represents an average density in the element and $\dot{Q}'''$ is the latent heat release rate by solidification:

$$\dot{Q}''' = \Delta H \cdot \left(\frac{\mathrm{d}V^{\mathrm{Eut}}}{\mathrm{d}t}\rho + \rho^{\gamma}\frac{\mathrm{d}f^{\gamma}}{\mathrm{d}t}V^{\mathrm{off}} + \rho^{\gamma}f^{\gamma}\frac{\mathrm{d}V^{\mathrm{off}}}{\mathrm{d}t}\right)\frac{1}{V^t} \tag{7}$$

where ΔH is the specific latent heat of the casting alloy and V^t is the element volume. Inserting the equation for $\frac{\mathrm{d}f^{\gamma}}{\mathrm{d}t}$ in $\dot{Q}'''$ and rearranging we have

$$\tilde{\rho c_p}\frac{\mathrm{d}T}{\mathrm{d}t} = k\nabla^2 T + \tilde{\dot{Q}}''' \qquad \text{with} \tag{8}$$

$$\tilde{\rho c_p} = \left(\rho c_p - \Delta H \rho^{\gamma}\frac{\Phi V^{\mathrm{off}}}{(1-k_C)w_C^l m_C^{\gamma}}\frac{1}{V^t}\right)$$

$$\tilde{\dot{Q}}''' = \Delta H \rho^{\gamma} \cdot \left(\frac{\mathrm{d}V^{\mathrm{Eut}}}{\mathrm{d}t} - \frac{X_C \cdot V^{\mathrm{off}}}{(1-k_C)w_C^l} + f^{\gamma}\frac{\mathrm{d}V^{\mathrm{off}}}{\mathrm{d}t}\right)\frac{1}{V^t}$$

Thus we include the latent heat released from the off-eutectic austenite when solving for the temperature, even though the amount of solidified material is yet unknown. After having calculated the rate of change of temperature the change in the off-eutectic austenite solid fraction can be obtained. Unless otherwise noted, the model constants are as in Ref. [4].

4. Validation of the model

A series of simulations was performed in order to obtain agreement between experimental data and simulations. The initial temperature of the melt in the simulation was set to 1325°C as this is the highest temperature registered in the experiment [6]. The nucleation parameter A_n was along the work of others, [7, 4], set to values around $A_n = 10^{11}$ m^{-3}K^{-1}. Since the three bars

were cast from the same melt, the parameters that are used for the melt must be the same for all three.

Figure 2 and 3 show the temperature at the centre of the casting as a function of time for each of the three bar sizes from experimental and simulated data. The figure for the 52 mm casting shows data for two values of A_n to illustrate the sensitivity of the cooling curve to this parameter as commented on below. The solidification times for the 34.7 mm and 52 mm castings are well reproduced in the simulated data despite too short eutectic plateaus which in the case of the 65 mm casting results in a solidification time that is too small. The figures also show that the initial cooling conditions seem to be well simulated for the 34.7 mm bar as there is a good correspondence between the initial slopes of the temperature curves, but as size increases the experimental data show faster cooling than the simulated. Further, the undercooling just before the eutectic plateau is not reproduced in any of the simulations.

The differences in the shapes of the cooling curves and in initial cooling rate might originate partly from imprecise modelling of the decrease of the mould's ability to extract heat from the casting. In green sand moulds this phenomenon is closely linked to the water evaporation and vapour transport as the mould heats up, [8], which might not be well modelled through a dependency on the fraction solid of the surface element as it is done in this study and also done conventionally. Further, as discussed by Pedersen et al. [4], it is assumed that there is no nucleation barrier for the formation of off-eutectic austenite in the model which might not be realistic. In the model, off-eutectic austenite will start forming as soon as the liquidus line is reached and thus the timing of the release of latent heat from this process might not be correct. This will contribute to differences between experiment and simulation.

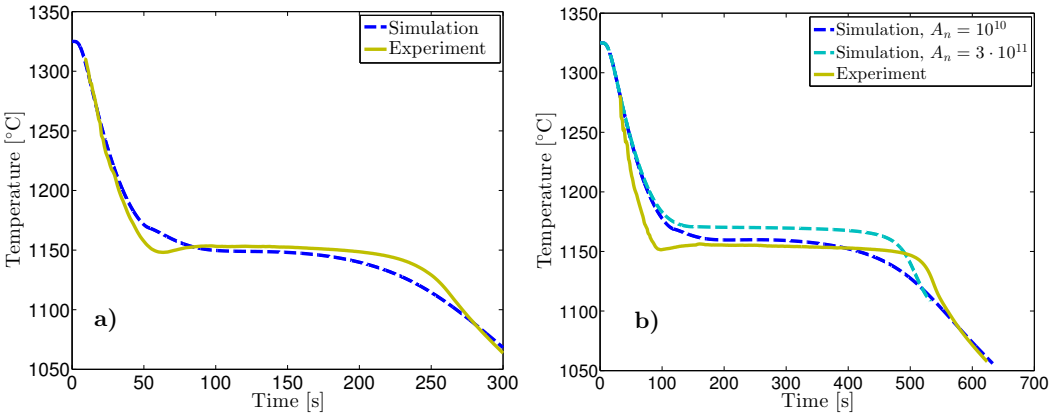

Figure 2. Temperature at the cross section centre of the **a)** 34.7 mm and **b)** 52 mm bars obtained by simulation and experiment. The initial cast temperature was 1325°C and the nucleation constant $A_n = 10^{10}$ m^{-3}K^{-1} for the 34.7 mm casting while results for $A_n = 3 \cdot 10^{11}$ m^{-3}K^{-1} were also included for the 52 mm case.

The nucleation constant A_n greatly influences the temperature of the eutectic plateau in this model and the results obtained using two different values are used to illustrate the following points. High values of A_n leads to a higher nucleation rate and thus to an increased amount of carbon removed from the liquid before reaching the austenite liquidus which will result in a higher temperature for the eutectic plateau on the cooling curve. This is illustrated by the curve for $A_n = 3 \cdot 10^{11}$ m^{-3}K^{-1} in the simulation of the 52 mm bar, Fig. 2 b). Thus, even though the simulations with $A_n = 10^{10}$ m^{-3}K^{-1} predict the level of the eutectic plateau quite accurately it is at the cost of using a quite low nucleation constant. This leads to low nodule number densities.

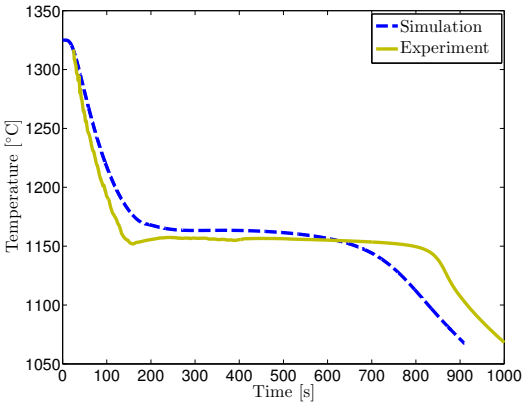

Figure 3. Temperature at the centre of the 65 mm bar cross section obtained by simulation and experiment. The initial cast temperature was 1325°C and the nucleation constant $A_n = 10^{10}$ m^{-3}K^{-1}.

Table 2 shows the nodule number densities from experiment and simulation at the centre and the upper right corner of the casting as seen from Fig. 1. Microscope images from the corner and the centre of the 52 mm casting is presented in Fig. 4. Degenerate graphite was found at the centre of both the 52 mm and the 65 mm casting. This observation will bias the nodule count from the centre as a single degenerate nodule will be segmented by the image analysis software as multiple individual nodules. This limits the value of the this data from the casting centre as basis for validation. The three dimensional size distribution was obtained from a two dimensional distribution using the Schwartz-Saltykov method [9].

The simulations with $A_n = 10^{10}$ m^{-3}K^{-1} predict much lower density than what was found from the experiment and this is a direct consequence of the low A_n as can be seen by comparing to the results with $A_n = 3 \cdot 10^{11}$ m^{-3}K^{-1} which show values comparable to those of the experiment. This at the same time raised the temperature of the eutectic plateau to 15°C above the experimental curve in the case of the 52 mm bar illustrating the trade off between a good fit to the cooling curve and to the nodule number density that has to be made with the present model.

Table 2. Nodule count (nodules pr m^3) at the centre of the castings compared to calculated nodule counts at the centre and near the corner of a casting cross section respectively. Data are from the 52 mm and 65 mm castings and only nodules with a diameter greater than 5 μm have been included.

	52 mm		**65 mm**	
	Corner	Centre	Corner	Centre
Experiment	$4.08 \cdot 10^{13}$	-	$2.22 \cdot 10^{13}$	-
Simulation $A_n = 10^{10}$ m^{-3}K^{-1}	$2.18 \cdot 10^{12}$	$1.34 \cdot 10^{12}$	$2.01 \cdot 10^{12}$	$1.20 \cdot 10^{12}$
Simulation $A_n = 3 \cdot 10^{11}$ m^{-3}K^{-1}	$3.91 \cdot 10^{13}$	$2.16 \cdot 10^{13}$	$3.97 \cdot 10^{13}$	$1.97 \cdot 10^{13}$

5. Solidification of thick-walled part

We have validated the model with reasonable success and now expand the simulation domain to contain a quarter of a bar with cross section of 300 mm by 300 mm to simulate the solidification of a thick-walled part. Even though the model does not include the formation

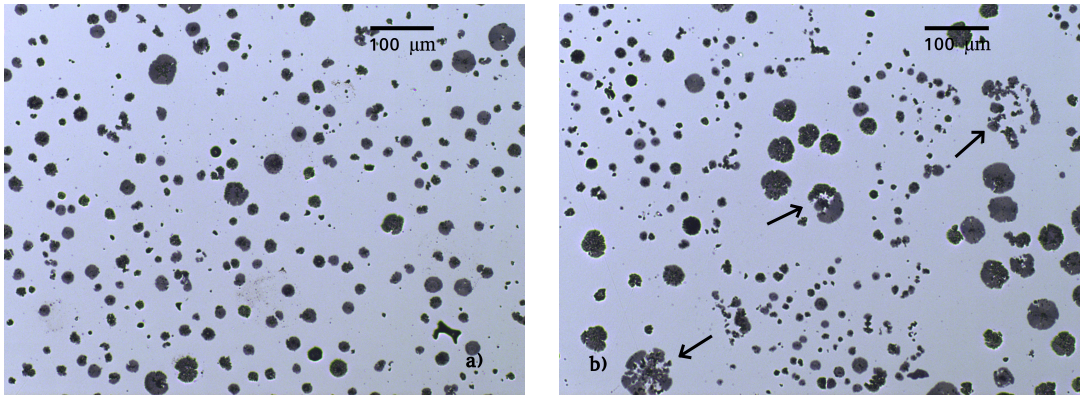

Figure 4. Example of graphite morphology from **a)** the corner and **b)** the centre from the 52 mm casting. Examples of degenerate graphite are marked with arrows.

of degenerate graphite morphologies and the cooling curves from castings involving degenerate graphite are affected by the formation of this type of graphite, [3], the fundamental features of the solidification pattern of thick-walled castings are likely to be the same.

Figure 5 shows the temperature and fraction solid in the elements along the diagonal of the cross section. The solidification starts by the formation of a solid shell at the interface to the mould which over time advances towards the centre of the casting. Initially, large temperature gradients exist throughout the casting but as the solidification proceeds a thermally homogeneous zone is established in the central part of the casting which to a large extend is still liquid. The central zone of the casting is maintained close to the eutectic temperature over long time intervals with only limited amount of solid present in the form of encapsulated nodules. As the formation of degenerate graphite is associated with low cooling rates the central zone in the thick-walled casting is indeed where one would expect degenerate graphite to form.

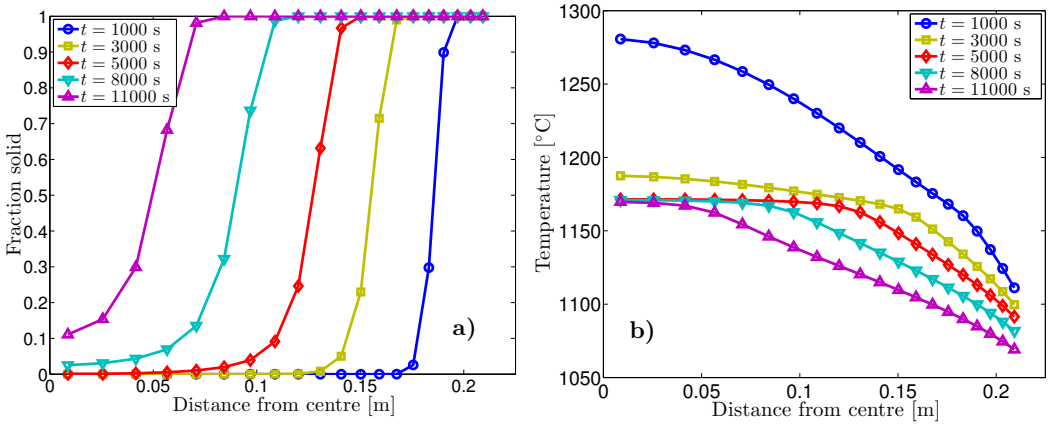

Figure 5. Fraction solid **a)** and temperature **b)** at different time points along the diagonal of the 300 mm bar cross section for $A_n = 10^{10}$ m^{-3}K^{-1}.

In Fig. 6 the temperature and fraction solid profiles along the diagonal of the 34.7 mm ba at various points in time are plotted as a comparison to Fig. 5. The 34.7 mm casting shows a distinctively different solidification pattern. While there is no clear solidification front in the 34.7 mm as large parts of the cross section are solidifying more or less simultaneously, the thick-walled 300 mm bar first creates a solid shell and then establishes a zone with only small

thermal gradients which solidify homogeneously. The 52 mm and 65 mm bars show elements of both solidification patterns by initially creating a solid shell leaving the centre of the castings to solidify simultaneously.

This corresponds well to the observation of degenerate graphite found at the centre of the 52 mm casting presented in Fig. 4 as low cooling rates promote the formation of this type of morphology. Also, analysis of the porosity distribution in the castings suggests shell formation in the 65 mm casting, [6], in agreement with the present simulations.

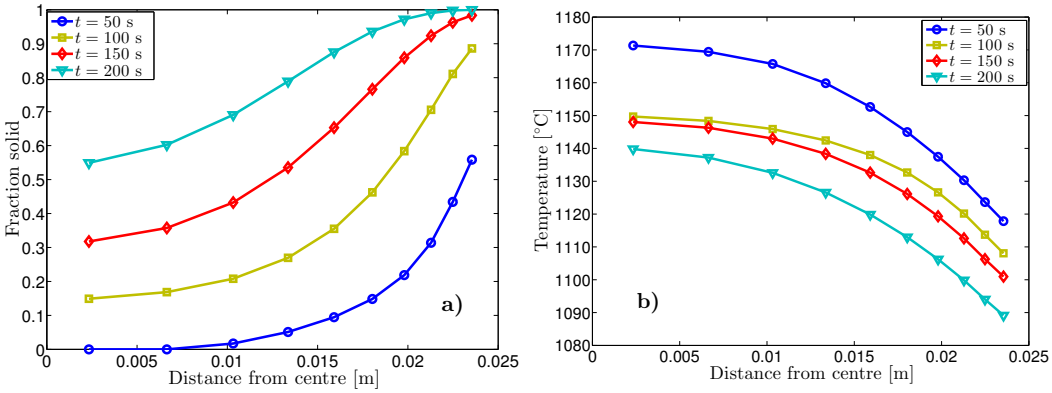

Figure 6. Fraction solid **a)** and temperature **b)** at different time points along the diagonal of the 34.7 mm bar cross section. The cooling curve for the centre of the casting is shown Fig. 2 a).

6. Conclusion

A solidification model for ductile cast iron was presented and the solidification castings of varying wall thicknesses was simulated. The simulation was validated against experimental data in terms of cooling curves and nodule number densities with reasonable agreement however also stressing the parameter sensitivity of the microstructural model applied. The analysis of the solidification pattern showed the formation of a long term thermally homogeneous zone at the centre of the thick-walled 300 mm by 300 mm casting with solidification only proceeding slowly from the edge towards the centre. The small 34.7 mm by 34.7 mm casting displayed a fundamentally different solidification pattern where no clear solidification front exists. The solidification pattern appears closely related to the development of the thermal gradients with thermally homogeneous zones associated with the centre of large castings relevant to the formation of porosities and degenerate graphite.

References

[1] Lesoult G, Castro M and Lacaze J 1998 *Acta Metallurgica* **46** 983–995
[2] Källbom R, Hamberg K and Björkegren L 2005 Chunky graphite formation and influence on mechanical properties in ductile cast iron *Component Design by Castings, VTT Symposium 237* (Espoo) pp 63–86
[3] Sertucha J, Suárez R, Asenjo I, Larrañaga P, Lacaze J, Ferrer I and Armendariz S 2009 *ISIJ International* **49** 220–228
[4] Pedersen K M, Hattel J H and Tiedje N 2006 *Acta Materialia* **54** 5103–5114
[5] Vedel-Smith N, Rasmussen J and Tiedje N 2015 *Journal of Materials Processing Technology* **217** 262–271 ISSN 09240136
[6] Vedel-Smith N K and Tiedje N S 2014 Feeding Against Gravity with Spot Feeders in High Silicon Ductile Iron *10th International Symposium on the Science and Processing of Cast Iron - SPCI10* (Mar Del Plata)
[7] Lacaze J, Castro M and Lesoult G 1998 *Acta Metallurgica* **46** 997–1010
[8] Kubo K and Pehlke R D 1986 *Metallurgical Transactions B* **17** 903–911
[9] Underwood E E 1970 *Quantitative Stereology* (Reading, Mass.: Addison-Wesley)